

Corotational Instability, Magnetic Resonances and Global Inertial-Acoustic Oscillations in Magnetized Black-Hole Accretion Discs

Wen Fu^{1*} and Dong Lai^{1,2*}

¹*Department of Astronomy, Cornell University, Ithaca, NY 14853, USA*

²*KITP, University of California, Santa Barbara, CA 93106, USA*

31 August 2010

ABSTRACT

Low-order, non-axisymmetric p-modes (also referred as inertial-acoustic modes) in hydrodynamic accretion discs around black holes are plausible candidates for high-frequency quasi-periodic oscillations (QPOs) observed in a number of accreting black-hole systems. These modes are trapped in the inner-most region of the accretion disc, and are subject to global instabilities due to wave absorption at the corotation resonance (where the wave pattern frequency ω/m equals the disc rotation rate Ω), when the fluid vortensity, $\zeta = \kappa^2/(2\Omega\Sigma)$ (where κ and Σ are the radial epicyclic frequency and disc surface density, respectively), has a positive gradient. We investigate the effects of disc magnetic fields on the wave absorption at corotation and the related wave super-reflection of the corotation barrier, and on the overstability of disc p-modes. In general, in the presence of magnetic fields, the p-modes have the character of inertial-fast magnetosonic waves in their propagation zone. For discs with a pure toroidal field, the corotation resonance is split into two magnetic resonances, where the wave frequency in the corotating frame of the fluid, $\tilde{\omega} = \omega - m\Omega$, matches the slow magnetosonic wave frequency. Significant wave energy/angular momentum absorption occurs at both magnetic resonances, but with opposite signs, such that one of them enhances the super-reflection while the other diminishes it. The combined effect of the two magnetic resonances is to reduce the super-reflection and the growth rate of the overstable p-modes. Our calculations show that even a subthermal toroidal field (with the magnetic pressure less than the gas pressure) may suppress the overstability of hydrodynamic ($B = 0$) p-modes. For accretion discs with mixed (toroidal and vertical) magnetic fields, two additional Alfvén resonances appear, where $\tilde{\omega}$ matches the local Alfvén wave frequency. The effect of these additional resonances is to further reduce or diminish the growth rate of p-modes. Our results suggest that in order for the non-axisymmetric p-modes to be a viable candidate for the observed high-frequency QPOs, the disc magnetic field must be appreciably subthermal, or other mode excitation mechanisms are at work.

Key words: accretion, accretion discs – hydrodynamics – MHD – waves – X-rays: binaries – black hole physics

1 INTRODUCTION

Quasi-periodic oscillations (QPOs) in black-hole (BH) X-ray binaries have been intensively studied since the launch of NASA’s *Rossini X-ray Timing Explorer* (Swank 1999). The observed QPOs can be divided into two classes. The low-frequency QPOs

* Email: wenfu@astro.cornell.edu; dong@astro.cornell.edu

(about 0.1–50 Hz) are common, observable when the systems are in the hard state and the steep power-law state (also called “very high state”; see Done et al. 2007). They typically have high amplitudes and high coherence ($Q \gtrsim 10$), and can vary in frequency on short timescales (minutes). The high-frequency QPOs (HFQPOs, 40–450 Hz), however, have only been observed in the steep power-law state in seven BH X-ray binaries. They typically have low amplitudes (0.5 – 2% rms at 2–60 keV) and low coherence ($Q \sim 2 - 10$), with small variations in frequency (less than $\sim 15\%$), and appear alone or in pairs with a frequency ratio close to 2:3 (see Remillard & McClintock 2006 for a review). QPOs in X-ray emission have also been detected in the active galaxy RE J1034+396 (Gierlinski et al. 2008; Middleton et al. 2009) as well as in several Ultra-Luminous X-ray sources (ULXs) (e.g., Strohmayer & Mushotzky 2009; Feng, Rao & Kaaret 2010). These are likely the “supermassive” or “massive” analogs of the QPOs detected in Galactic BH X-ray binaries (see Middleton & Done 2010).

It is widely accepted that HFQPOs are associated with the dynamics of BH accretion flows near the Inner-most Stable Circular Orbit (ISCO). Beyond this general consensus, the physical origin of HFQPOs remains unclear, despite their well-defined phenomenology. In recent years, a number of models/theories with various degrees of sophistication have been proposed to explain HFQPOs [see Sec. 1 of Lai & Tsang 2009 (hereafter LT09) for a review of most of the existing models]. Of particular interest to the present paper is the relativistic diskoseismic oscillation model, in which general relativity (GR) effects produce trapped oscillation modes in the inner region of the disc (e.g., Okazaki et al. 1987; Nowak & Wagoner 1991; see Wagoner 1999 and Kato 2001 for reviews). One can divide various diskoseismic modes according to their vertical structures (see Fig. 1 of Fu & Lai 2009): The so-called p-modes (also called inertial-acoustic modes) have zero node in their wavefunctions along the vertical direction, while the g-modes (also known as inertial modes or inertial-gravity modes)¹ have at least one vertical nodes². Diskoseismic g-modes have received wide theoretical attentions because they can be trapped by the GR effect without relying on special inner disc boundary conditions (Okazaki et al. 1987), and they may be resonantly excited by global disc deformations (warp and eccentricity) through nonlinear effects (Kato 2003b, 2008; Ferreira & Ogilvie 2008). Kato (2003a) and Li, Goodman & Narayan (2003) (see also Zhang & Lai 2006 and Latter & Balbus 2009) showed that the non-axisymmetric g-mode that contains a corotation resonance (CR, where the wave pattern frequency ω/m equals the background rotation rate Ω ; here ω is the mode frequency and m is the azimuthal mode number) in the wave zone is heavily damped (see Tsang & Lai 2009a for a similar study for the c-modes). Thus the only non-axisymmetric g-modes of interest are those trapped around the maximum of the $(\Omega + \kappa/m)$ profile (where κ is the radial epicyclic frequency). However, the frequencies of such modes, $\omega \simeq m\Omega(r_{\text{ISCO}})$, are too high (by a factor of 2–3) compared to the observed values, given the measured mass and the estimated spin parameter of the BH (Silbergleit & Wagoner 2008; Tassev & Bertschinger 2007). Another potential problem with the g-modes is that their trapping zones (which arise from the maximum of the κ profile near the ISCO) can be destroyed by a weak (sub-thermal) magnetic field (Fu & Lai 2009). For example, the cavity of the $m = 0$ g-mode for a non-spinning BH vanishes when $B_z^2/(4\pi\rho c_s^2) \gtrsim 0.1$ (where B_z is the vertical magnetic field, ρ is the density and c_s is the sound speed). This elimination of the g-mode cavity is probably the reason for the disappearance of g-modes in recent MHD simulations (O’Neill, Reynolds & Miller 2009). Moreover, several numerical simulations suggest that g-modes may not survive vigorous disc turbulence driven by magneto-rotational instabilities (MRI) (e.g. Arras, Blaes & Turner 2006; Reynolds & Miller 2009).

The focus of this paper is on p-modes. In an unmagnetized disc, non-axisymmetric p-modes are trapped between the inner disc edge (at the ISCO) and the inner Lindblad resonance (ILR) radius (where $\tilde{\omega} = \omega - m\Omega = -\kappa$). So the existence of global p-modes does require a partially reflective inner disc boundary (see LT09). LT09 showed that such non-axisymmetric p-modes can be overstable for two reasons: (1) Because the spiral density waves inside the ILR carry negative energies while those outside the outer Lindblad resonance (OLR) (where $\tilde{\omega} = \kappa$) carry positive energies, the leakage of the p-mode energy when the wave tunnels through the corotation barrier (between ILR and OLR) leads to mode growth. (2) More importantly, p-modes can become overstable due to wave absorption at the corotation resonance (CR, where $\tilde{\omega} = 0$). Near the BH, the radial epicyclic frequency κ reaches a maximum before decreasing to zero at the ISCO. This causes a non-monotonic behavior in the fluid vortensity, $\zeta = \kappa^2/(2\Sigma\Omega)$ (where Σ is the surface density of the disc), such that $d\zeta/dr > 0$ inside the radius where ζ peaks. It can be shown that the sign of the corotational wave absorption depends on the sign of $d\zeta/dr$ (Tsang & Lai 2008; LT09; see also Goldreich & Tremaine 1979)³. Thus, p-modes with positive vortensity gradient at the corotation radius can grow in amplitudes due to corotational wave absorption. The resulting overstable non-axisymmetric p-modes were suggested to offer a possible explanation for HFQPOs (LT09; Tsang & Lai 2009b).

Realistic BH accretion disks are expected to contain appreciable magnetic fields as a result of the nonlinear development

¹ Note that other than similar mathematical forms of dispersion relations, disk g-modes have no relation to stellar g-modes which are driven by buoyancy.

² The so-called c-modes (corrugation modes) also have at least one vertical node, but they have low frequencies and are not relevant to HFQPOs.

³ This applies to barotropic discs, for which the pressure is a function of the density ρ only. For a disc with radial stratification, the radial entropy gradient affects wave absorption at the CR (see Lovelace et al. 1999; Baruteau & Masset 2008), and one can define an effective vortensity, $\zeta_{\text{eff}} = \zeta/S^{2/\Gamma}$ (where $S = P/S^{\Gamma}$ and Γ is the 2-dimensional adiabatic index), that plays a similar role as ζ (see Tsang & Lai 2009b).

of the MRI (e.g., Balbus & Hawley 1998). Starting from Hawley et al. (1995), Brandenburg et al. (1995) and Stone et al. (1996) in the 1990s, the property of the MRI turbulence have been studied using numerical simulations under different conditions and setups (local shearing box with/without vertical stratification, with/without explicit viscosity and resistivity, different equations of state, global simulations; e.g., Miller & Stone 2000; Hirose et al. 2009; Guan et al. 2009; Simon et al. 2009; Davis et al. 2010; Fromang 2010; Longaretti & Lesur 2010; Sorathia et al. 2010). Although the precise mechanism of the nonlinear saturation of the MRI remains unclear (see Pessah & Goodman 2009), the simulations generally show that turbulent discs are dominated by large-scale toroidal fields approaching (but less than) equipartition, with somewhat smaller poloidal fields. Therefore, it is important to understand how magnetic fields change the characters of the CR and the overstability of BH disc p-modes. These are the main issues we will address in this paper.

We have recently shown (Fu & Lai 2009), based on local analysis of diskoseismic waves, that the propagation diagram of p-modes, (particularly the wave zone between inner disc edge (at r_{ISCO}) and the ILR are not significantly modified by disc magnetic fields. Thus, we expect that the p-mode frequencies in a magnetic disc are not much different from those in a zero-field disc. However, the effect of magnetic field on the corotational wave absorption is more complicated. As we will see, for a pure toroidal field, the CR is split into two *magnetic slow resonances*, where the Doppler-shifted mode frequency $\tilde{\omega}$ matches the frequency of slow MHD waves propagating along the field line (see Sakurai et al. 1991; Goossens et al. 1992; Terquem 2003). With a mixed (poloidal and toroidal) magnetic field, two additional *Alfvén resonances* appear, where $\tilde{\omega}$ matches the Alfvén frequency associated with the toroidal field (Keppens et al. 2002). Thus, in general, the original CR is split into four resonances (the inner/outer magnetic slow resonances and the inner/outer Alfvén resonances), which exhibit a rather rich and complex dynamical behavior.

We note that Tagger and collaborators (Tagger & Pellat 1999; Varniere & Tagger 2002; Tagger & Varniere 2006) developed the theory of accretion-ejection instability for discs containing large-scale poloidal magnetic fields with strengths of order equipartition. Most of their analysis were restricted to vertical fields threading an infinitely thin disc with vacuum outside. They showed that the long-range behavior of the perturbed vacuum field outside the disc greatly enhances the overstability of non-axisymmetric disc oscillation modes. It is currently unclear whether the magnetic field configurations adopted by Tagger et al. can be realized by MRI turbulence – such field configuration may be produced by magnetic field advection from large radii (e.g. Lovelace et al. 2009). It is also unclear if the accretion-ejection instability is robust when more general disc field configurations are assumed. By contrast, in this paper we focus on the effects of magnetic fields *inside* the disc. Since the p-modes we are interested in have no vertical structure (i.e., $k_z = 0$), our disc model is essentially a cylinder, with the unperturbed disc properties (e.g., the density ρ , sound speed c_s , rotation Ω and magnetic fields B_ϕ and B_z) depending only on r (the cylindrical radius). While the magnetic field configurations considered in this paper are prone to MRI, the p-modes are not *directly* affected by the MRI because $k_z = 0$.

Our paper is organized as follows. In Sec. 2, we introduce the equilibrium state of the disc and general MHD equations with comments on the equation structure. We present in Sec. 3 the effective potential of wave propagations for different magnetic field configurations. Section 4 examines how super-reflection across the corotation barrier is modified by the magnetic field. We present numerical calculations of global p-modes of magnetized BH accretion discs in Sec. 5 and conclude in Sec. 6.

2 SETUP AND BASIC EQUATIONS

We consider a non-self-gravitating accretion disc, satisfying the usual ideal MHD equations

$$\frac{\partial \rho}{\partial t} + \nabla \cdot (\rho \mathbf{v}) = 0, \quad (1)$$

$$\frac{\partial \mathbf{v}}{\partial t} + (\mathbf{v} \cdot \nabla) \mathbf{v} = -\frac{1}{\rho} \nabla \Pi - \nabla \Phi + \frac{1}{4\pi \rho} (\mathbf{B} \cdot \nabla) \mathbf{B}, \quad (2)$$

$$\frac{\partial \mathbf{B}}{\partial t} = \nabla \times (\mathbf{v} \times \mathbf{B}), \quad (3)$$

where ρ , P , \mathbf{v} are the fluid density, pressure and velocity, Φ is the gravitational potential, and

$$\Pi \equiv P + \frac{\mathbf{B}^2}{8\pi} \quad (4)$$

is the total pressure. The magnetic field \mathbf{B} also satisfies the equation $\nabla \cdot \mathbf{B} = 0$. We assume the flow obeys the barotropic equation of state $P = P(\rho)$.

We adopt the cylindrical coordinates (r, ϕ, z) which are centered on the central BH and have the z -axis in the direction perpendicular to the disc plane. The unperturbed background disc has a velocity field $\mathbf{v} = r\Omega(r)\hat{\phi}$, and the magnetic field consists of both toroidal and vertical components $\mathbf{B} = B_\phi(r)\hat{\phi} + B_z(r)\hat{z}$. The gravitational acceleration in radial direction is defined as

$$g = \frac{d\Phi}{dr} \quad (5)$$

so that $-\nabla\Phi = -g\hat{\mathbf{r}}$ and $g = r\Omega_K^2 > 0$, where Ω_K is the angular frequency for a test mass (the Keplerian frequency)⁴. Thus the radial force balance equation reads

$$\rho g = \rho r\Omega^2 - \frac{d\Pi}{dr} - \frac{B_\phi^2}{4\pi r}. \quad (6)$$

To probe the dynamical properties of the magnetized flow, we apply linear perturbations to the ideal MHD Eqs. (1)-(3) by assuming the perturbation of any physical variable f to have the form $\delta f \propto e^{im\phi - i\omega t}$ with m being the azimuthal mode number and ω the wave frequency. The background flow and magnetic field have no z -dependence and we will assume that the perturbation also has no z -dependence ($k_z = 0$). The resulting linearized perturbation equations clearly contain variables $\delta\mathbf{v}$, $\delta\rho$, δP , $\delta\Pi$ and $\delta\mathbf{B}$. To simplify the algebra, we define a new variable

$$\delta h = \frac{\delta\Pi}{\rho} = \frac{\delta P}{\rho} + \frac{\mathbf{B} \cdot \delta\mathbf{B}}{4\pi\rho}. \quad (7)$$

Using $\Delta\mathbf{v} = \delta\mathbf{v} + \boldsymbol{\xi} \cdot \nabla\mathbf{v} = d\boldsymbol{\xi}/dt = -i\omega\boldsymbol{\xi} + (\mathbf{v} \cdot \nabla)\boldsymbol{\xi}$, we find that the Eulerian perturbation $\delta\mathbf{v}$ is related to the Lagrangian displacement vector $\boldsymbol{\xi}$ by $\delta\mathbf{v} = -i\tilde{\omega}\boldsymbol{\xi} - r\Omega'\xi_r\hat{\boldsymbol{\phi}}$ (prime denotes radial derivative). Also, we have (for barotropic flow)

$$\delta\rho = \delta P/c_s^2 \quad (8)$$

with $c_s = \sqrt{dP/d\rho}$ being the sound speed. Therefore, we can express all the perturbation quantities in terms of ξ_r and δh , then further combine the perturbation equations into two equations for these two variables:

$$\frac{d\xi_r}{dr} = A_{11}\xi_r + A_{12}\delta h, \quad (9)$$

$$\frac{d\delta h}{dr} = A_{21}\xi_r + A_{22}\delta h, \quad (10)$$

where

$$A_{11} = \frac{r\tilde{\omega}^2 [(\omega_{A\phi}^2 - \Omega^2)\tilde{\omega}^2 + \omega_{A\phi}^2\omega^2]}{(c_s^2 + v_A^2)(\tilde{\omega}^2 - m^2\omega_{A\phi}^2)(\tilde{\omega}^2 - \omega_s^2)} + \frac{g\tilde{\omega}^2}{(c_s^2 + v_A^2)(\tilde{\omega}^2 - \omega_s^2)} - \frac{\tilde{\omega}^2 + 2m\tilde{\omega}\Omega + m^2\omega_{A\phi}^2}{r(\tilde{\omega}^2 - m^2\omega_{A\phi}^2)}, \quad (11)$$

$$A_{12} = -\frac{\tilde{\omega}^4}{(c_s^2 + v_A^2)(\tilde{\omega}^2 - m^2\omega_{A\phi}^2)(\tilde{\omega}^2 - \omega_s^2)} + \frac{m^2}{r^2(\tilde{\omega}^2 - m^2\omega_{A\phi}^2)}, \quad (12)$$

$$A_{21} = \tilde{\omega}^2 - m^2\omega_{A\phi}^2 - \frac{4(m\omega_{A\phi}^2 + \tilde{\omega}\Omega)^2}{\tilde{\omega}^2 - m^2\omega_{A\phi}^2} + r\frac{d}{dr}(\omega_{A\phi}^2 - \Omega^2) + (\omega_{A\phi}^2 - \Omega^2)\frac{r}{\rho}\frac{d\rho}{dr} + \frac{g}{\rho}\frac{d\rho}{dr} \\ + \frac{1}{(c_s^2 + v_A^2)(\tilde{\omega}^2 - m^2\omega_{A\phi}^2)(\tilde{\omega}^2 - \omega_s^2)} \left\{ r [(\omega_{A\phi}^2 - \Omega^2)\tilde{\omega}^2 + \omega_{A\phi}^2\omega^2] + g(\tilde{\omega}^2 - m^2\omega_{A\phi}^2) \right\}^2, \quad (13)$$

$$A_{22} = -\frac{r\tilde{\omega}^2 [(\omega_{A\phi}^2 - \Omega^2)\tilde{\omega}^2 + \omega_{A\phi}^2\omega^2]}{(c_s^2 + v_A^2)(\tilde{\omega}^2 - m^2\omega_{A\phi}^2)(\tilde{\omega}^2 - \omega_s^2)} - \frac{g\tilde{\omega}^2}{(c_s^2 + v_A^2)(\tilde{\omega}^2 - \omega_s^2)} + \frac{2m(m\omega_{A\phi}^2 + \tilde{\omega}\Omega)}{r(\tilde{\omega}^2 - m^2\omega_{A\phi}^2)} - \frac{1}{\rho}\frac{d\rho}{dr}. \quad (14)$$

In the above expressions,

$$\tilde{\omega} = \omega - m\Omega \quad (15)$$

is the wave frequency in the co-rotating frame,

$$v_A = \frac{|\mathbf{B}|}{\sqrt{4\pi\rho}} \quad (16)$$

is the Alfvén velocity,

$$\omega_{A\phi} = \frac{v_{A\phi}}{r} = \frac{B_\phi}{r\sqrt{4\pi\rho}} \quad (17)$$

is the toroidal Alfvén frequency, and

$$\omega_s = \frac{c_s}{\sqrt{c_s^2 + v_A^2}} m\omega_{A\phi} = k_\phi \frac{c_s v_{A\phi}}{\sqrt{c_s^2 + v_A^2}}, \quad (18)$$

is the slow magnetosonic wave frequency for $\mathbf{k} = (m/r)\hat{\boldsymbol{\phi}}$.

Equations (9)-(10) describe the linear perturbations (without vertical wavenumber) in a compressible 2D flow threaded by a mixture of toroidal and vertical magnetic fields. In the hydrodynamic disc limit ($B \rightarrow 0$), they reduce to the related equations in Goldreich & Tremaine (1979) with no external forcing potential [see also Tsang & Lai 2008 (TL08 hereafter)

⁴ Here ‘‘Keplerian’’ does not necessarily mean the gravitational potential is Newtonian. See the end of Sec. 2.

and LT09]. They also agree with system (14) in Blokland et al. (2005)⁵ in the $k_z \rightarrow 0$ and barotropic limit, although their equations are cast on slightly different variables ($\delta\Pi$ instead of δh). The Hameiri-Bondeson-Iacono-Bhattacharjee (HBIB) type of equations presented in Blokland et al. (2005) have been derived before by Hameiri (1981) and Bondeson et al. (1987) [see also Mikhailovskii et al. (2009); Goossens et al. (1992) (hereafter GHS92) and reference therein] for a magnetized rotating flow in the absence of external gravity. The equations including gravity were obtained by Keppens et al. (2002) (hereafter KCP02) using the same Frieman-Rosenbluth technique (Frieman & Rosenbluth 1960). System (5) in KCP02 is by far the most general formulation (with finite B_ϕ , B_z , m , k_z , v_ϕ , v_z and adiabatic equation of state) that in principle governs all the MHD waves and instabilities for a compressible MHD fluid with an equilibrium flow in cylindrical geometry. In this paper, we focus on the effects of magnetic fields on the corotational instability of the inertial-acoustic modes (p-modes) in accretion discs, thus Eqs. (9)-(10) are our main working equations. Recently, Yu & Li (2009) considered a similar system (with finite k_z and pure toroidal B field) to study the Rossby wave instability and they obtained equations with similar structure as Eqs. (9)-(10). Our equations in the pure toroidal B field limit ($B_z \rightarrow 0$) are the same as theirs in the $k_z \rightarrow 0$ limit. Also, the disc system that we study here are similar to the one considered by Terquem (2003), where instead of solving for global modes the author looked into the interaction between the disc and a planet and the consequences on planet migrations.

Evidently, the coefficients in Eqs. (11)-(14) are singular when

$$\tilde{\omega}^2 = m^2 \omega_{A\phi}^2, \quad (19)$$

and

$$\tilde{\omega}^2 = \omega_s^2. \quad (20)$$

In more general situations (with $k_z \neq 0$), $m\omega_{A\phi}$ in Eq. (19) generalizes to $(\mathbf{k} \cdot \mathbf{B})/\sqrt{4\pi\rho}$, which is the Alfvén frequency, and the slow magnetosonic frequency ω_s generalizes to $\sqrt{c_s^2/(c_s^2 + v_A^2)}(\mathbf{k} \cdot \mathbf{B})/\sqrt{4\pi\rho}$. Following Sakurai et al. (1991) and KCP02, we shall call (19) the *Alfvén Resonance* (AR) and (20) the *Magnetic slow Resonance* (MR). Note that these singularities/resonances have also been studied in the specific context of disc-planet interactions. Terquem (2003) considered a 2D disk with a pure toroidal magnetic field and found that a subthermal toroidal B-field is capable of stopping the inward planetary migration as long as the $B_\phi(r)$ gradient is negative enough. This analytic finding was later confirmed by 2D MHD simulation results (Fromang et al. 2005). On the other hand, Muto et al. (2008), by employing shearing sheet approximation, performed 3D (i.e., $k_z \neq 0$) calculations for a disk with a pure poloidal magnetic field and showed that type I planetary migration could be outward if the B-field is strong enough (superthermal).

In the special case of $k_z = B_z = 0$, Eq. (19) is no longer a real singularity of the differential equations. In this case, one can show, through some subtle mathematical manipulations, that the terms $\tilde{\omega}^2 - m^2 \omega_{A\phi}^2$ in A_{11} , A_{12} , A_{21} and A_{22} all get canceled. These four coefficients then reduce to

$$A_{11} = \frac{v_{A\phi}^2}{c_s^2 + v_{A\phi}^2} \frac{1}{\tilde{\omega}^2 - \omega_s^2} \left[\frac{\tilde{\omega}^2}{r} - \frac{m^2 c_s^2}{r^3} - \frac{c_s^2}{v_{A\phi}^2} \frac{\tilde{\omega}^2 + 2m\tilde{\omega}\Omega}{r} - \frac{\tilde{\omega}^2}{v_{A\phi}^2} (r\Omega^2 - g) \right], \quad (21)$$

$$A_{12} = -\frac{1}{v_{A\phi}^2 + c_s^2} \frac{\tilde{\omega}^2 - m^2 c_s^2/r^2}{\tilde{\omega}^2 - \omega_s^2}, \quad (22)$$

$$A_{21} = \tilde{\omega}^2 - m^2 \omega_{A\phi}^2 - \kappa^2 - \frac{d \ln(\rho r/B_\phi^2)}{d \ln r} \frac{v_{A\phi}^2}{c_s^2 + v_{A\phi}^2} (\Omega^2 - g/r - 2c_s^2/r^2) - \frac{1}{\tilde{\omega}^2 - \omega_s^2} \left\{ 4\Omega^2 \omega_s^2 + \left[\frac{mv_{A\phi}^2}{c_s^2 + v_{A\phi}^2} (\Omega^2 - g/r + 2c_s^2/r^2) \right]^2 + 4m\tilde{\omega}\Omega \frac{v_{A\phi}^2}{c_s^2 + v_{A\phi}^2} (\Omega^2 - g/r + 2c_s^2/r^2) \right\}, \quad (23)$$

$$A_{22} = \frac{m}{r} \frac{c_s^2}{c_s^2 + v_{A\phi}^2} \frac{1}{\tilde{\omega}^2 - \omega_s^2} \left[2\tilde{\omega}\Omega + \frac{mv_{A\phi}^2}{c_s^2 + v_{A\phi}^2} (\Omega^2 - g/r + 2c_s^2/r^2) \right] - \frac{d \ln \rho}{d \ln r} + \frac{1}{c_s^2 + v_{A\phi}^2} (r\Omega^2 - g - 2v_{A\phi}^2/r), \quad (24)$$

where the radial epicyclic frequency κ is given by

$$\kappa = \left[\frac{2\Omega}{r} \frac{d}{dr} (r^2 \Omega) \right]^{1/2}. \quad (25)$$

This peculiar disappearance of Alfvén singularity can also be verified from a different perspective. GHS92 derived the jump conditions for ξ_r and $\delta\Pi$ (called P' in their paper) across the Alfvén resonance

$$[\xi_r] \propto g_B = mB_z/r - k_z B_\phi,$$

$$[\delta\Pi] \propto B_z$$

⁵ There is a typo in their Eq. (20), where in the last line, the term $(B_\theta^2 \tilde{\omega} + Fv_\theta)$ should be $(B_\theta^2 \tilde{\omega} + Fv_\theta)^2$.

(see their Eqs. [42]-[43]). We see that when $k_z = B_z = 0$, both ξ_r and $\delta\Pi$ are continuous across the Alfvén resonance, thus the Alfvén singularity disappears⁶. In a non-magnetic disc, Eqs. (19)-(20) reduce to the corotation singularity (TL08).

In Sec. 3 and Sec. 4, we will simply employ Newtonian gravitational potential, which has free-particle orbital frequency $\Omega_K \propto r^{-3/2}$ and epicyclic frequency $\kappa = \Omega_K$. This way a dimension-free analysis can be easily made without missing the essential physics. However, in Sec. 5, in order to make a direct comparison with results in LT09, we will use the Paczynski-Wiita pseudo-Newtonian potential (Paczynski & Wiita 1980)

$$\Phi = -\frac{GM}{r - r_s}, \quad (26)$$

where M is the central BH mass and $r_s = 2GM/c^2$ is the Schwarzschild radius. The corresponding free-particle orbital frequency and radial epicyclic frequency are

$$\Omega_K = \left(\frac{1}{r} \frac{d\Phi}{dr}\right)^{1/2} = \sqrt{\frac{GM}{r}} \frac{1}{r - r_s}, \quad (27)$$

$$\kappa = \Omega_K \sqrt{\frac{r - 3r_s}{r - r_s}}. \quad (28)$$

Note that κ^2 peaks at $r = (2 + \sqrt{3})r_s$ and decreases to zero at $r = 3r_s$. Throughout this paper, we will consider thin discs with the sound speed $c_s \ll r\Omega_K$ and magnetic field satisfying $B^2/(4\pi\rho) \ll (r\Omega_K)^2$, so that $\Omega \simeq \Omega_K$.

3 EFFECTIVE POTENTIAL AND WAVE PROPAGATION DIAGRAM

We can combine Eqs. (9)-(10) into a single second-order differential equation on δh

$$\frac{d^2}{dr^2} \delta h + C_1(r) \frac{d}{dr} \delta h + C_0(r) \delta h = 0, \quad (29)$$

where

$$C_1(r) = -A_{11} - A_{22} - \frac{1}{A_{21}} \frac{dA_{21}}{dr}, \quad (30)$$

$$C_0(r) = A_{11}A_{22} - A_{12}A_{21} - \frac{dA_{22}}{dr} + \frac{A_{22}}{A_{21}} \frac{dA_{21}}{dr}. \quad (31)$$

We introduce a new variable

$$\eta = \exp \left[\int^r \frac{1}{2} C_1(r) dr \right] \delta h, \quad (32)$$

so that Eq. (29) can be rewritten as a wave equation for η :

$$\frac{d^2 \eta}{dr^2} - V(r) \eta = 0, \quad (33)$$

where

$$V(r) = \frac{1}{4} C_1(r)^2 + \frac{1}{2} \frac{dC_1(r)}{dr} - C_0(r) \quad (34)$$

is the effective potential for wave propagation. Considering a local plane wave solution

$$\eta \propto \exp \left[i \int^r k_r(s) ds \right], \quad (35)$$

Eq. (33) then yields

$$k_r^2 = -V(r). \quad (36)$$

Formally, wave can propagate only in the region with $V(r) < 0$. Our derivation above is quite general and can be applied to complicated systems as the details have all been captured in the four coefficients A_{ij} . Figures 1-3 show the effective potential for various situations discussed below.

⁶ Although the analysis in GHS92 does not consider external gravity, one can show that the effect of gravity can be easily included through replacing the term $\rho v_\phi^2/r$ in their Eq. (5) by $\rho v_\phi^2/r + \rho g$. This modification only changes the relations between the background variables (B_ϕ , v_ϕ , c_s , etc.) The jump conditions for ξ_r and P' would remain the same.

3.1 Hydrodynamical discs

For a non-magnetic disc, the four coefficients A_{ij} simplify to

$$A_{11} = -\frac{d \ln(r\rho)}{dr} - \frac{2m\Omega}{r\tilde{\omega}}, \quad (37)$$

$$A_{12} = -\frac{1}{c_s^2} + \frac{m^2}{r^2\tilde{\omega}^2}, \quad (38)$$

$$A_{21} = -D, \quad (39)$$

$$A_{22} = \frac{2m\Omega}{r\tilde{\omega}}, \quad (40)$$

where $D = \kappa^2 - \tilde{\omega}^2$. Thus $C_0(r)$ and $C_1(r)$ now read

$$C_0(r) = -\frac{D}{c_s^2} - \frac{m^2}{r^2} - \frac{2m\Omega}{r\tilde{\omega}} \left(\frac{d}{dr} \ln \frac{\Omega\rho}{D} \right), \quad (41)$$

$$C_1(r) = -\frac{d}{dr} \ln \frac{D}{r\rho}. \quad (42)$$

The effective potential then takes the following form

$$V(r) = \frac{D}{c_s^2} + \frac{m^2}{r^2} + \frac{2m\Omega}{r\tilde{\omega}} \left(\frac{d}{dr} \ln \frac{\Omega\rho}{D} \right) + S^{1/2} \frac{d^2}{dr^2} S^{-1/2}, \quad (43)$$

where $S = D/(r\rho)$. The effective potential $V(r)$ is singular at both the corotation resonance (CR), where $\tilde{\omega} = 0$, and the Lindblad resonances (LRs), where $D = 0$ (see Figs. 1-3). However, the singularities at the LRs are spurious singularities of the wave equation (i.e. they can be removed by rewriting the equation in alternative variables [e.g., Narayan et al. 1987; TL08]) and only the CR is a non-removable singularity. The behavior of $V(r)$ around the CR depends on $d\zeta/dr$ (evaluated at the corotation radius r_c), the gradient of the background fluid vortensity, ζ , defined by

$$\zeta = \frac{\kappa^2}{2\Omega\rho}. \quad (44)$$

For $d\zeta/dr < 0$ a narrow ‘‘Rossby wave zone’’ lies just inside r_c , while for $d\zeta/dr > 0$ the Rossby zone lies just outside r_c ; in the special case of $d\zeta/dr = 0$, the corotation singularity disappears (see TL08).

3.2 Discs with pure toroidal magnetic fields

As mentioned in Sec. 2, for a disc with a pure toroidal magnetic field, the CR splits into two magnetic slow resonances (MRs). This can be seen clearly from the wave propagation diagram shown in Figs. 1-3. For $B = 0$, the effective potentials reduce to those shown in TL08. In the upper panels of Figs. 1-3, we see that for small magnetic fields (with $\omega_{A\phi} \ll \Omega$), the effective potential profile is not affected much by the B-field except near the corotation. The blow-ups in the bottom panels show that the toroidal magnetic field splits the CR into two MRs, the inner magnetic resonance (IMR) and outer magnetic resonance (OMR), one on each side of the CR. A larger toroidal field (see the long-dashed lines) gives a wider radial separation between the MRs and a shallower potential well around r_c . Note that independent of the sign of $(d\zeta/dr)_c$, there always exists an effective wave zone centered around corotation point and bounded by the two MRs.

Far away from the resonances (the regions on the left and right sides of the upper panels of Figs. 1-3), the WKB dispersion relation (36) reduces to (see Terquem 2003; Fu & Lai 2009)

$$\tilde{\omega}^2 = \kappa^2 + k_r^2(c_s^2 + v_{A\phi}^2). \quad (45)$$

This describes fast magnetosonic waves modified by the disc rotation. Thus the spiral density waves (inertial-acoustic waves) inside the ILR and outside the OLR are inertial-fast magnetosonic waves.

The behavior of the effective potential around the MRs is more difficult to analyze. The IMR and OMR are separated from the CR by the distance

$$r_{\text{mr}} - r_c \simeq \pm \left(\frac{2\omega_s}{3m\Omega} \right) r_c, \quad (46)$$

(the upper sign is for the OMR and the lower sign for the IMR). Because of the complexity of the equations involved, no simple analytical expression for $V(r)$ can be derived, even in the asymptotic limit (e.g., $\tilde{\omega} \rightarrow \pm\omega_s$ and $v_{A\phi}/r\Omega \ll 1$). Nevertheless, a careful examination of Eqs. (21)-(24), (30)-(31), (34) and numerical calculation of $V(r)$ show that in the neighborhood of the MRs, the effective potential can be written in the following form:

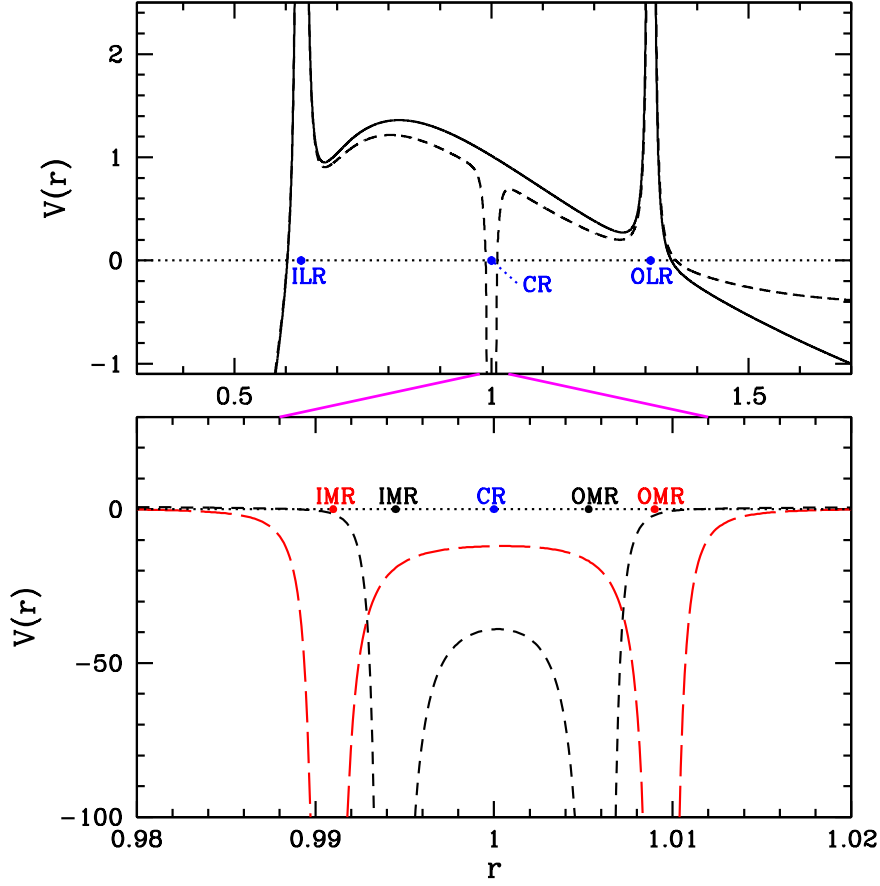


Figure 1. Wave propagation diagram in accretion discs when the background fluid vortensity gradient (evaluated at the corotation resonance radius) $(d\zeta/dr)_c = 0$. In the upper panel, the solid line shows the effective potential $V(r)$ as a function of r for $B = 0$ discs, and the dashed line shows $V(r)$ for discs with finite toroidal magnetic fields. Waves can propagate only in the region where $V(r) < 0$. The labels ILR, OLR and CR denote the inner Lindblad resonance, outer Lindblad resonance and corotation resonance, respectively. The lower panel shows the blow-up of the region near the CR (located at $r_c = 1$), and the long-dashed line shows the case with a stronger B_ϕ than the short-dashed line. The labels IMR and OMR denote the inner magnetic (slow) resonance and outer magnetic resonance, respectively. Note that the vertical scales in the upper and bottom panels differ by a large factor. A Newtonian potential is used in calculating $V(r)$. (A color version of this figure is available in the online journal.)

$$V(r) = f_0 + \frac{f_1}{\tilde{\omega}^2 - \omega_s^2} + \frac{f_{2+}}{(\tilde{\omega} - \omega_s)^2} + \frac{f_{2-}}{(\tilde{\omega} + \omega_s)^2}, \quad (47)$$

where f_0 , f_1 , $f_{2\pm}$ vary slowly around the CR/MRs region. Thus, the effective potential is dominated by second-order singularities at the MRs, i.e., $V(r) \propto (r - r_{\text{mr}})^{-2}$ (see Figs. 1-3). The coefficients $f_{2\pm}$ can be calculated numerically, and some examples of how f_{2+} and f_{2-} depend the magnetic field strength are shown in Fig. 4. We see that in dimensionless units (with $G = M = r_c = 1$, $m = 2$ and $c_s \ll r\Omega$, $v_{A\phi} \ll r\Omega$), both f_{2+} and f_{2-} are negative and approximately equal to -2 . Thus, near one of the MRs (e.g., the OMR), we have $k_r^2 = -V(r) \sim 2/(\tilde{\omega} - \omega_s)^2 \sim 0.2/(r - r_{\text{mr}})^2$, or $k_r \sim 0.4/|r - r_{\text{mr}}|$. Since k_r^2 is smaller than $|dk_r/dr|$, the WKB analysis is not really valid near the MRs. On the other hand, close to the CR radius ($r = r_c$), we have $V(r) \sim -4/\omega_s^2$, which implies $k_r \sim 2\omega_s^{-1}$. Since the separation between the IMR and OMR is $2\omega_s/3\Omega$ (for $m = 2$), we find that the WKB phase variation across the CR region (but avoiding the MRs) is of order unity. Therefore, despite the deep effective potential at the MRs, physically there is not much a wave zone around the MRs/CR region. This feature is borne out in our numerical calculations of global wave modes presented in Sec. 5.

It is worth noting with the second-order singularities associated with the MRs, the $B \rightarrow 0$ limit is approached in a non-trivial way. From Fig. 4, we see that as the magnetic field decreases, f_{2+} and f_{2-} reach the same values ($\simeq -2.25$). Thus the singularities associated with $f_{2+}/(\tilde{\omega} - \omega_s)^2$ and $f_{2-}/(\tilde{\omega} + \omega_s)^2$ simply become $1/\tilde{\omega}^2$ as $B \rightarrow 0$. On the other hand, f_1 can be written as $f_1 = f_{10}\tilde{\omega}^0 + f_{11}\tilde{\omega} + f_{12}\tilde{\omega}^2 + \dots$, with f_{1i} being near constant around the MRs. As $B \rightarrow 0$, we have $f_{10} + f_{2+} + f_{2-} = 0$, and the second-order singularity term ($\propto 1/\tilde{\omega}^2$) in $V(r)$ disappears. What is left is the term $f_{11}/\tilde{\omega}$, a

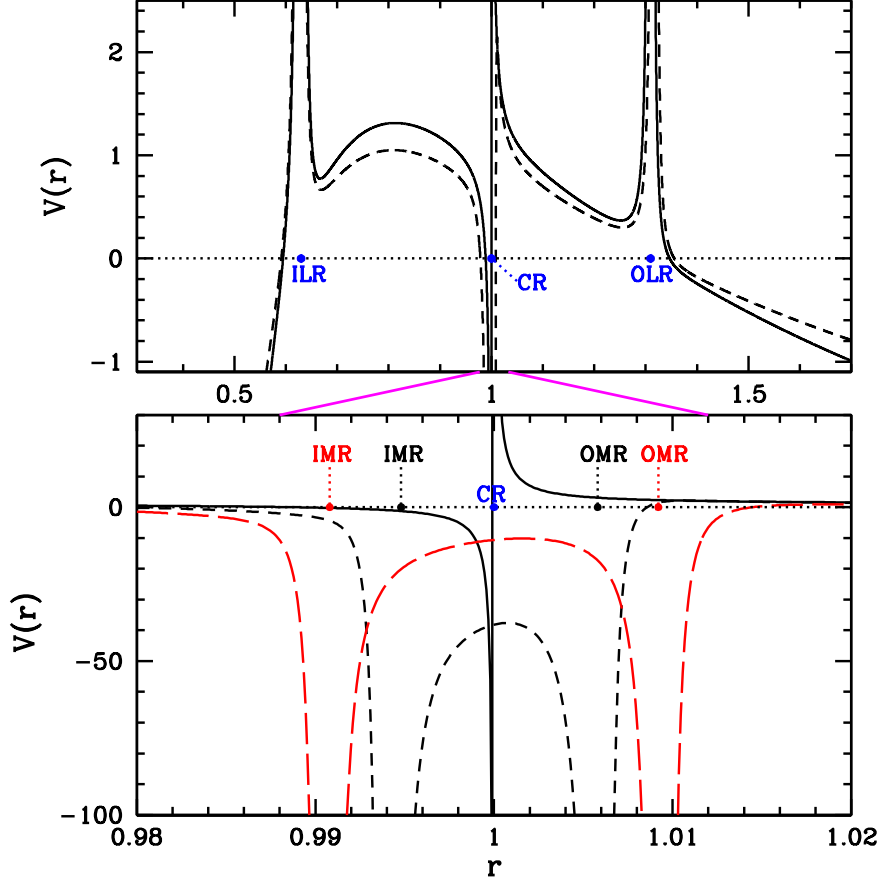


Figure 2. Same as Fig. 1, except for the case $(d\zeta/dr)_c < 0$.

first-order singularity associated with the CR in a non-magnetic disc. Evidently, as $B \rightarrow 0$, f_{11} is proportional to the vorticity gradient, $d\zeta/dr$.

3.3 Discs with pure vertical magnetic fields

Before examining the case of mixed magnetic fields, it is useful to consider discs with pure vertical fields. Here we assume that B_z is constant (independent of r) to simplify the analysis. The coefficients A_{ij} of the wave equations (9)-(10) are

$$A_{11} = -\frac{c_s^2}{c_s^2 + v_A^2} \frac{d \ln \rho}{dr} - \frac{2m\Omega}{r\tilde{\omega}} - \frac{1}{r}, \quad (48)$$

$$A_{12} = -\frac{1}{c_s^2 + v_A^2} + \frac{m^2}{r^2\tilde{\omega}^2}, \quad (49)$$

$$A_{21} = \tilde{\omega}^2 - \kappa^2 - \frac{c_s^2 v_A^2}{c_s^2 + v_A^2} \left(\frac{d \ln \rho}{dr} \right)^2, \quad (50)$$

$$A_{22} = -\frac{v_A^2}{c_s^2 + v_A^2} \frac{d \ln \rho}{dr} + \frac{2m\Omega}{r\tilde{\omega}}. \quad (51)$$

We then have

$$C_1 = -\frac{d}{dr} \ln \left(\frac{A_{21}}{r\rho} \right), \quad (52)$$

$$C_0 = -\frac{D}{c_s^2 + v_A^2} - \frac{m^2}{r^2} - \frac{2m\Omega}{r\tilde{\omega}} \left(\frac{d}{dr} \ln \frac{\Omega\rho^\lambda}{A_{21}} \right)$$

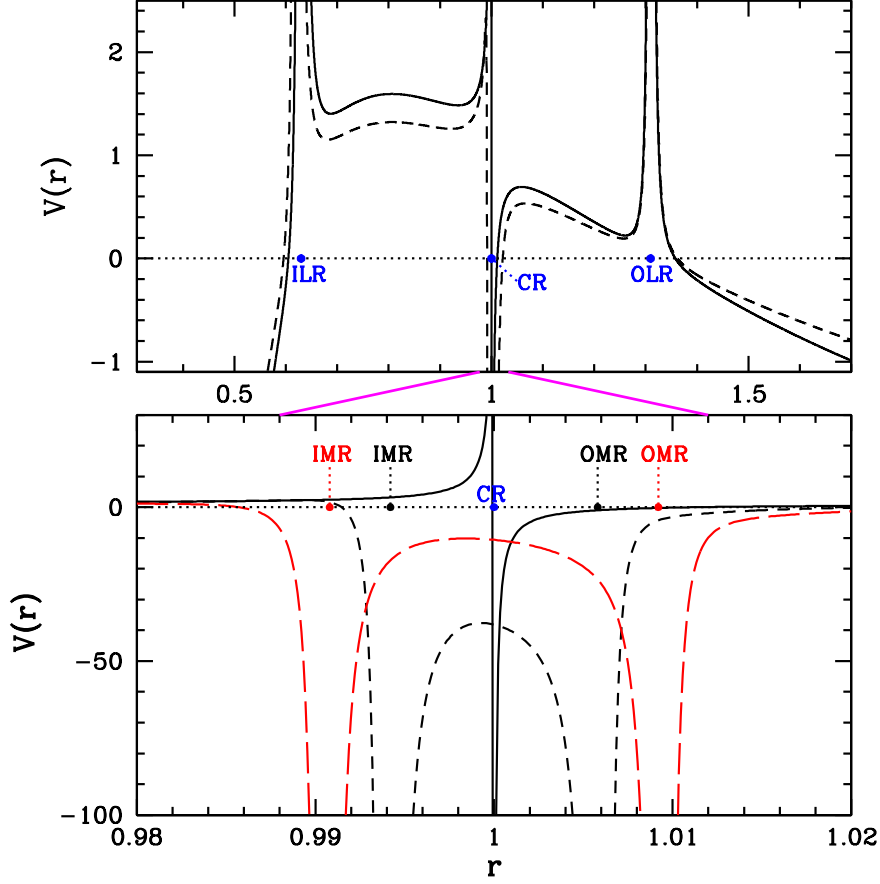


Figure 3. Same as Fig. 1, except for the case $(d\zeta/dr)_c > 0$.

$$+ \frac{m^2}{r^2 \tilde{\omega}^2} \frac{c_s^2 v_A^2}{c_s^2 + v_A^2} \left(\frac{d \ln \rho}{dr} \right)^2 - \frac{v_A^2}{c_s^2 + v_A^2} \left(\frac{d \ln \rho}{dr} \right) \left(\frac{d \ln(A_{21}/r)}{dr} \right) + \frac{d}{dr} \left(\frac{v_A^2}{c_s^2 + v_A^2} \frac{d \ln \rho}{dr} \right), \quad (53)$$

where

$$\lambda = (c_s^2 - v_A^2)/(c_s^2 + v_A^2) \quad (54)$$

and $D = \kappa^2 - \tilde{\omega}^2$. The resulting effective potential reads

$$V(r) = \frac{D}{c_s^2 + v_A^2} + \frac{m^2}{r^2} + \frac{2m\Omega}{r\tilde{\omega}} \left(\frac{d}{dr} \ln \frac{\Omega \rho^\lambda}{A_{21}} \right) + S^{1/2} \frac{d^2}{dr^2} S^{-1/2} - \frac{m^2}{r^2 \tilde{\omega}^2} \frac{c_s^2 v_A^2}{c_s^2 + v_A^2} \left(\frac{d \ln \rho}{dr} \right)^2 + \frac{v_A^2}{c_s^2 + v_A^2} \left(\frac{d \ln \rho}{dr} \right) \left(\frac{d \ln(A_{21}/r)}{dr} \right) - \frac{d}{dr} \left(\frac{v_A^2}{c_s^2 + v_A^2} \frac{d \ln \rho}{dr} \right), \quad (55)$$

where $S = A_{21}/(r\rho)$. Compared with the $V(r)$ in the $B = 0$ case, we see that a constant vertical field does not split the CR. However, in contrast to the first-order corotation singularity ($1/\tilde{\omega}$) in the $B = 0$ case, the CR in discs with $B_z \neq 0$ manifests mainly as a second-order singularity ($\sim 1/\tilde{\omega}^2$).

3.4 Discs with mixed magnetic fields

For a disc with mixed magnetic fields, the expression for the effective potential $V(r)$ is more complicated than the pure toroidal field case. In Fig. 5, we show a sketch of $V(r)$ when both B_z and B_ϕ are non-zero. We see that in addition to the two MRs (IMR and OMR) (already present in the pure toroidal field case), two Alfvén resonances (ARs) appear when $\tilde{\omega} = \pm m\omega_{A\phi}$. Since $m\omega_{A\phi} > \omega_s$, these ARs lie farther away from the corotation radius than the MRs, at the distance

$$r_{\text{ar}} - r_c = \pm \left(\frac{2\omega_{A\phi}}{3\Omega} \right) r_c. \quad (56)$$

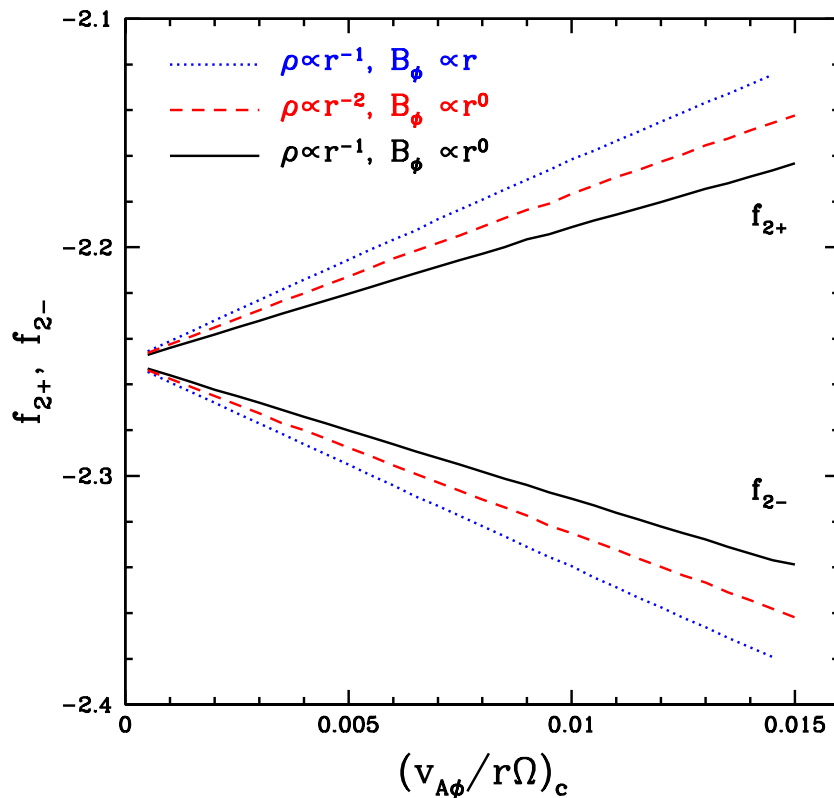


Figure 4. Numerical values of f_{2+} and f_{2-} [see Eq. (47)] as a function of the dimensionless ratio $v_{A\phi}/(r\Omega)$ (evaluated at $r = r_c$), which specifies the toroidal magnetic field strength in the disc. Dimensionless units are adopted, where $G = M = r_c = 1$, $m = 2$, and $c_s/(r\Omega) \ll 1$. Different line types represent different disc density and magnetic field profiles.

Unlike the MRs, the ARs are first-order singularities of the wave equation, i.e., $V(r) \propto 1/(\tilde{\omega} - m\omega_{A\phi}) \propto 1/(r - r_{\text{ar}})$ near the ARs.

4 SUPER-REFLECTION OF THE COROTATION BARRIER

As shown in Sec. 3, away from the CR/MRs/ARs region, the WKB dispersion relation is simply

$$\tilde{\omega}^2 = \kappa^2 + k_r^2(c_s^2 + v_A^2). \quad (57)$$

Thus waves can propagate either inside the ILR (where $\tilde{\omega} = -\kappa$) or outside the OLR (where $\tilde{\omega} = \kappa$), and the region between the ILR and OLR represents the “corotation barrier”, where waves are evanescent except for various possible singularities associated with the CR/MRs/ARs. We will be interested in the wave modes trapped between the disc inner edge and ILR. As in the hydrodynamic ($B = 0$) case, the growth rates of such p-modes depend directly on the wave reflectivity of the corotation barrier (TL08, LT09).

Consider launching a density wave $\delta h \propto \exp(-i \int^r k_r dr)$ from a radius inside the ILR ($r < r_{\text{ILR}}$) (assuming $k_r > 0$; the minus sign arises from the fact that group velocity and phase velocity have different signs where $r < r_{\text{ILR}}$, see TL08). The wave carries negative energy since its pattern speed ω/m is smaller than background rotation rate Ω . When the wave impinges on the corotation barrier, it is partly bounced back as a reflection wave $\delta h_{\text{R}} \propto \mathcal{R} \exp(i \int^r k_r dr)$, which carries negative energy, and partly transmitted through the evanescent zone and travels beyond the OLR as a transmission wave $\delta h_{\text{T}} \propto \mathcal{T} \exp(i \int^r k_r dr)$, which carries positive energy. \mathcal{R} and \mathcal{T} are reflection and transmission coefficients, respectively (see TL08). Let the net absorption of wave energy at the CR, MRs and ARs be \mathcal{D}_{abs} . Energy conservation then implies

$$|\mathcal{R}|^2 = 1 + |\mathcal{T}|^2 + \mathcal{D}_{\text{abs}}. \quad (58)$$

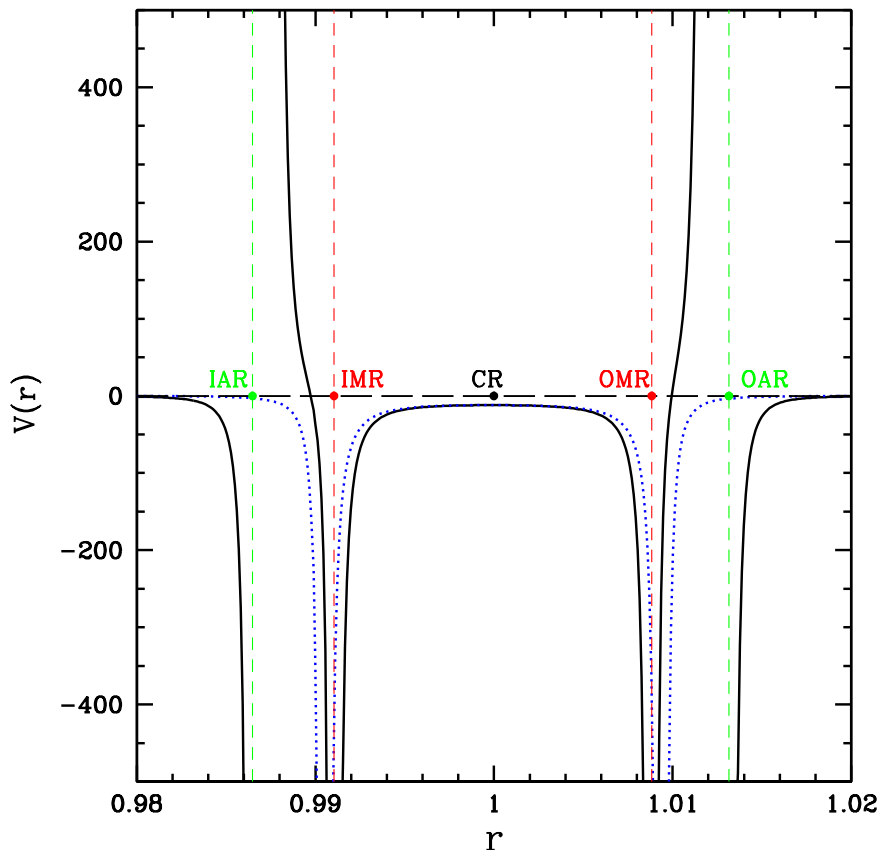


Figure 5. Effective potential around the corotation/magnetic resonance region for a disc with mixed magnetic fields (solid line). The dotted line shows $V(r)$ for the case with a pure toroidal field. The corotation resonance (CR), inner/outer magnetic (slow) resonances (IMR and OMR) and inner/outer Alfvén resonances (IAR and OAR) are indicated. Note that the MRs represent second-order singularities in $V(r)$, while the ARs (which exist only for the mixed field case) are first-order singularities.

Obviously, wave transmission through the corotation barrier (the $|\mathcal{T}|^2$ term) always tends to increase $|\mathcal{R}|^2$ beyond unity. However, the resonant wave absorption term \mathcal{D}_{abs} can be either positive or negative.

4.1 Non-magnetic Discs

TL08 showed that, for a $B = 0$ barotropic disc, the wave super-reflection ($|\mathcal{R}|^2 - 1$) is dominated by the corotational wave absorption, which depends on the dimensionless parameter

$$\nu = \left(\frac{c_s}{p\kappa} \frac{d}{dr} \ln \zeta \right)_c = \frac{2}{3} \beta \left(\sigma - \frac{3}{2} \right), \quad (59)$$

where ζ is the vortensity [see Eq. (44)], β , p and σ are defined by $\beta = c_s/(r\Omega)$, $\Omega \propto r^{-p}$ and $\rho \propto r^{-\sigma}$ (around the CR), respectively, and the subscript “c” implies that the quantity is evaluated at $r = r_c$. The second equality in Eq. (59) assumes (Newtonian) Keplerian discs ($p = 3/2$). Importantly, the corotational wave absorption is proportional to ν or $d\zeta/dr$. This can be understood from the fact that for $\nu > 0$ ($\nu < 0$), the Rossby zone lies outside (inside) r_c (see Figs. 1-3), implying a positive (negative) wave energy absorption. Thus, if neglecting $|\mathcal{T}|^2$, we have

$$|\mathcal{R}| - 1 \propto \nu \propto \left(\frac{d\zeta}{dr} \right)_c. \quad (60)$$

Tsang & Lai (2009b) further generalizes the analysis to non-barotropic flows with radial stratification, in which case an effective vortensity (which depends on the radial entropy profile of the disc) plays a similar role as ζ .

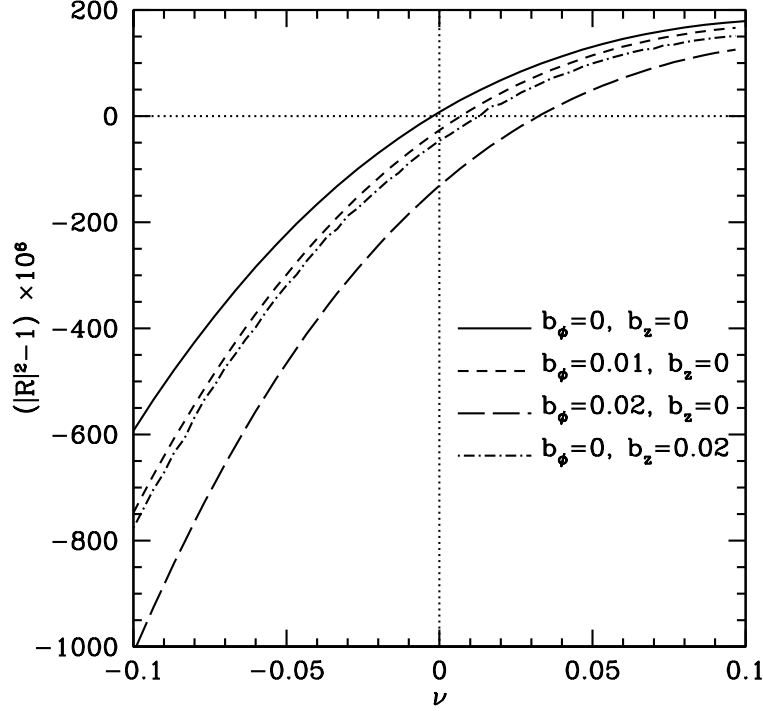


Figure 6. Reflection coefficient as a function of ν for a Newtonian Keplerian disk. Different lines represent different magnetic field strengths, measured by the dimensionless parameters $b_\phi = (v_{A\phi}/r\Omega)_c$ and $b_z = (v_{Az}/r\Omega)_c$. The other parameters are $m = 2$, $B_\phi \propto B_z \propto r^q$ with $q = 0$ and $\beta = c_s/(r\Omega) = 0.1$. The parameter ν is defined according to Eq. (59).

4.2 Numerical calculations of reflectivity

For discs with magnetic fields, we are not able to derive analytical expressions for the reflectivity. Thus we calculate \mathcal{R} numerically.

For definiteness, we consider a (Newtonian) Keplerian disc with

$$\Omega = \kappa \propto r^{-3/2}, \quad \rho \propto r^{-\sigma}, \quad B_\phi \propto B_z \propto r^q, \quad \frac{c_s}{r\Omega} = \beta, \quad (61)$$

where σ , q and β are constants. The strength of the field is characterized by the ratio $b_\phi = v_{A\phi}/(r\Omega)$ and $b_z = v_{Az}/(r\Omega)$, evaluated at r_c . We choose the wave frequency $\omega = \omega_r + i\omega_i$, with $0 < \omega_i \ll \omega_r$. The transmitted wave outside the OLR takes the form

$$\delta h \propto A \exp\left(i \int^r k_r dr\right), \quad (62)$$

where $k_r > 0$ is given by Eq. (36) or approximately by Eq. (45), and $A(r)$ can be obtained from Eq. (32) with $\eta \propto k_r^{-1/2}$. Thus the boundary condition at $r_{\text{out}} > r_{\text{OLR}}$ is

$$\left. \frac{d\delta h}{dr} \right|_{r_{\text{out}}} = \delta h (ik_r + A'/A) \Big|_{r_{\text{out}}}, \quad (63)$$

where $A' = dA/dr$. Starting from $r = r_{\text{out}}$, we integrate Eqs. (9)-(10) inwards to a radius inside the ILR. At $r = r_{\text{in}} < r_{\text{ILR}}$, the wavefunction has the form

$$\delta h \propto A \left[\exp\left(-i \int^r k_r dr\right) + \mathcal{R} \exp\left(i \int^r k_r dr\right) \right]. \quad (64)$$

The reflectivity \mathcal{R} can then be extracted from the equation

$$|\mathcal{R}| = \left| \frac{(-ik + A'/A)\delta h - \delta h'}{(ik + A'/A)\delta h - \delta h'} \right|_{r_{\text{in}}}. \quad (65)$$

In practice, at r_{in} (r_{out}) sufficiently inside r_{ILR} (outside r_{OLR}), the A'/A term can be dropped since $k_r \gg |A'/A|$.

Figure 6 shows the numerical results of the reflection coefficient as a function of ν , defined by Eq. (59). For $B = 0$, our result recovers that obtained by TL08. We see even a relatively weak (sub-thermal, with $v_{A\phi} \lesssim c_s$) toroidal field can significantly affect the reflectivity. As the magnetic field increases, the reflectivity decreases regardless of the sign of ν . A finite vertical field has a similar effect, although it is sub-dominant compared to the toroidal field effect. We will show in the following section that this result is consistent with the stability property of global disc p-modes.

5 GLOBAL P-MODES OF BLACK-HOLE ACCRETION DISCS

In this section, we present our calculations of the global non-axisymmetric p-modes in BH accretion discs. Recall that for a nonmagnetic disc, these are the inertial-acoustic modes partially trapped between the inner disc edge (at $r_{\text{in}} = r_{\text{ISCO}}$) and the ILR. For a disc with finite magnetic fields, these become inertial-fast magnetosonic waves.

We employ the standard shooting method (Press et al. 1992) to solve Eqs. (9)-(10) for the complex eigenfrequency $\omega = \omega_r + i\omega_i$. The boundary condition at $r_{\text{out}} > r_{\text{OLR}}$ is the outgoing-radiative condition discussed in Sec. 4.2 [see Eq. (63)]. At the inner boundary $r_{\text{in}} = r_{\text{ISCO}}$, we apply a free surface boundary condition,

$$\Delta h = \Delta \Pi / \rho = 0, \quad (66)$$

i.e., the Lagrangian perturbation of the total pressure vanishes. This boundary condition corresponds to a idealized situation in which no wave energy is lost at the inner disc radius. As discussed in LT09 (and references therein), the inner edge of a real BH disc is more complicated and may involve wave energy loss due to radial infall of the accreting gas. Since our focus here is to understand how disc magnetic fields affect the corotational instability, we will adopt the simple boundary condition (66) for all the numerical calculations presented in this section.

As mentioned in Sec. 2, we use the Paczynski-Wiita pseudo-Newtonian potential [Eq. (26)] to mimic the GR effect. The disk density profile and magnetic field profile take the power-law forms

$$\rho \propto r^{-\sigma}, \quad B_\phi \propto B_z \propto r^q. \quad (67)$$

The thermal effect and the magnetic field effect are characterized by the dimensionless parameters

$$\beta = \frac{c_s}{r\Omega}, \quad b_\phi = \frac{v_{A\phi}}{r\Omega} \Big|_{r_{\text{in}}}, \quad b_z = \frac{v_{Az}}{r\Omega} \Big|_{r_{\text{in}}}, \quad (68)$$

with β being constant.

The angular momentum flux carried by the wave across the magnetized disc is given by (e.g. Pessah et al. 2006)

$$F(r) = \pi r^2 \rho \text{Re}(\delta v_r \delta v_\phi^*) - \frac{1}{4} r^2 \text{Re}(\delta B_r \delta B_\phi^*), \quad (69)$$

where * denotes complex conjugate. The first and second terms in (69) are related to the Reynolds stress and Maxwell stress, respectively. The solution of Eqs. (9)-(10) gives $\xi_r(r)$ and $\delta h(r)$. The expressions for δv_r , δv_ϕ , δB_r and δB_ϕ can be derived from the original linearized perturbation equations (1)-(3):

$$\delta v_r = -i\tilde{\omega}\xi_r, \quad (70)$$

$$\delta v_\phi = \left(-\frac{\kappa^2}{2\Omega} - \frac{m\omega_{A\phi}^2}{\tilde{\omega}} + \frac{mv_{A\phi}^2}{r\tilde{\omega}} A_{11} \right) \xi_r + \left(\frac{m}{r\tilde{\omega}} + \frac{mv_{A\phi}^2}{r\tilde{\omega}} A_{12} \right) \delta h, \quad (71)$$

$$\delta B_r = \frac{imB_\phi}{r} \xi_r, \quad (72)$$

$$\delta B_\phi = \left(-q\frac{B_\phi}{r} - A_{11}B_\phi \right) \xi_r - A_{12}B_\phi \delta h. \quad (73)$$

5.1 Results for discs with pure toroidal magnetic fields

Figure 5.1 gives an example of the eigenfunctions for overstable p-modes in magnetized BH accretion discs. For comparison, the corresponding results for a $B = 0$ disc are also shown. Clearly, with a small B field ($b_\phi \ll 1$), the wavefunctions away from the corotation/magnetic resonances (CR/MRs) are only slightly modified. The wave action is still trapped in the inner disc region. The most noticeable effects occur near the MRs, where both δh and δv_r experience significant variations. In this example, the $B = 0$ disc has $d\zeta/dr > 0$ at the CR, so that corotational wave absorption leads to a mode growth rate $\omega_i \simeq 0.0027\Omega_{\text{in}}$. The inclusion of a small toroidal B field, $b_\phi = 0.01$ [corresponding to $(v_{A\phi}/r\Omega)_c = 0.0175$], however, reduces the mode growth rate to $\omega_i \simeq 0.0018\Omega_{\text{in}}$. Note that the disc sound speed in the example is $c_s = 0.1r\Omega$, so the $b_\phi = 0.01$ corresponds to $(v_{A\phi}/c_s)_c = 0.175$.

The origin of the diminished mode growth rate due to magnetic fields can be understood by examining the angular

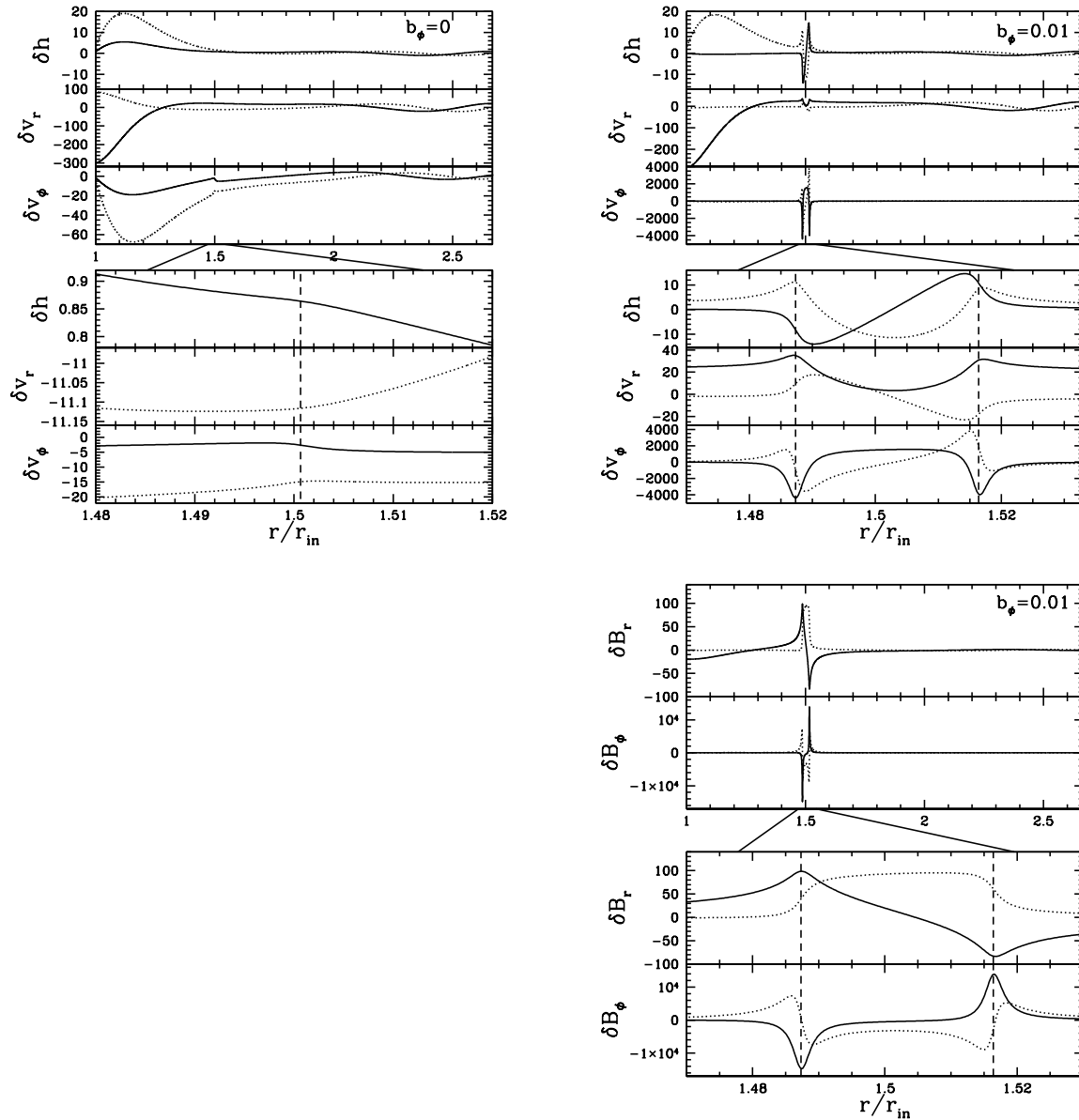


Figure 7. Example wavefunctions of $m = 2$ p-modes in BH accretion discs. The disc density profile is $\rho \propto r^{-1}$ (i.e., $\sigma = 1$) and the sound speed is $c_s = 0.1r\Omega$ (i.e., $\beta = 0.1$). The left columns are for a $B = 0$ disc, with the eigenvalue $\omega = (0.9324 + i0.0027)\Omega_{\text{in}}$ (where Ω_{in} is the disc rotation rate at $r = r_{\text{in}} = r_{\text{ISCO}}$); the right panels are for a disc with $b_\phi = (v_{A\phi}/r\Omega)_{\text{in}} = 0.01$ [corresponding to $(v_{A\phi}/r\Omega)_c = 0.0175$] (with B_ϕ independent of r , i.e., $q = 0$), with $\omega = (0.9312 + i0.0018)\Omega_{\text{in}}$. In each subfigure, the upper panels show different variables as a function of r in the full fluid zone. The solid and dotted lines depict the real and imaginary parts, respectively. The bottom panels zoom in the region near the corotation resonance, with the vertical lines indicating the locations of the CR (left) and magnetic slow resonances (right). The vertical scales of the wavefunctions are arbitrary, with $\delta h(r_{\text{out}}) = 1$.

momentum flux carried by the wave modes. Figure 8 gives some examples. We see that in the $B = 0$ case, there is a jump of the angular momentum flux across the CR,

$$\Delta F = F(r_{c-}) - F(r_{c+}), \quad (B = 0). \quad (74)$$

The fact that $\Delta F > 0$ implies a positive wave energy (angular momentum) absorbed at the CR [i.e., $\mathcal{D}_{\text{abs}} > 0$ in Eq. (58)]; this leads to super-reflection and is the main driver for the overstability of hydrodynamic p-modes. For discs with a finite B_ϕ , the CR is split into two MRs (the IMR and OMR), and we see from Fig. 8 that significant flux jumps occur at both the IMR and OMR. The flux jump at the IMR, $\Delta F_{\text{IMR}} = F(r_{\text{IMR}-}) - F(r_{\text{IMR}+})$, is negative, implying a negative angular momentum absorption. The flux jump at the OMR, $\Delta F_{\text{OMR}} = F(r_{\text{OMR}-}) - F(r_{\text{OMR}+})$, however, is positive, implying a positive angular momentum absorption. The net angular momentum jump across the MRs region is then

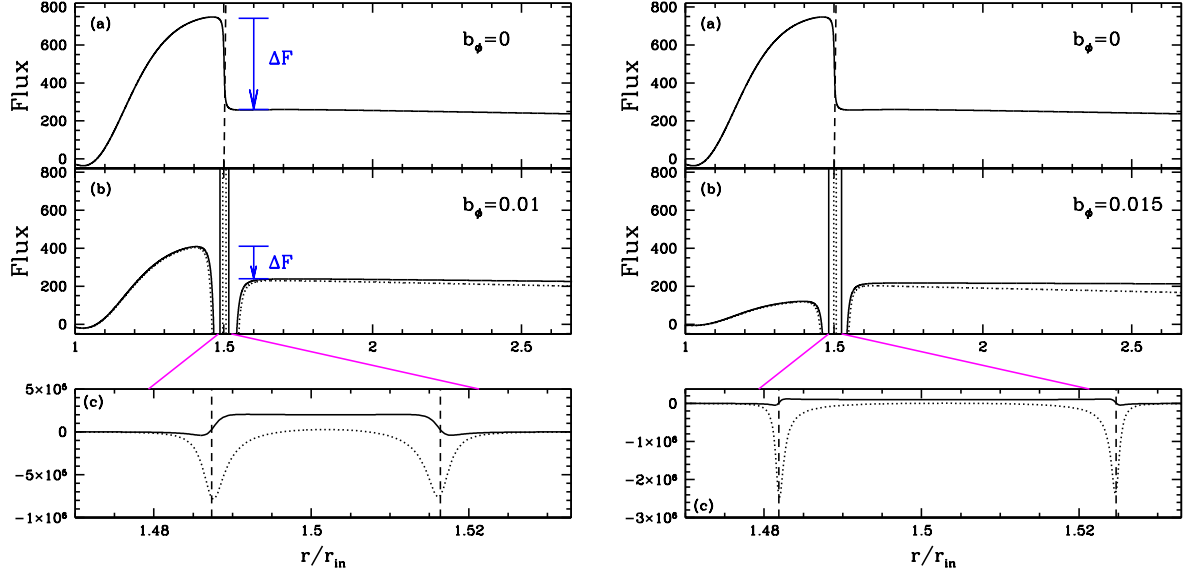


Figure 8. Angular momentum flux carried by the wave as a function of r . The disc parameters are $\sigma = 1$, $q = 0$ and $\beta = 0.1$, and the wave modes have $m = 2$. Panel (a) shows the result of a $B = 0$ disc [with the mode frequency $\omega = (0.9324 + i0.0027)\Omega_{\text{in}}$] with the vertical line indicating the corotation resonance. Panel (b) is for a magnetized disc with $b_\phi = 0.01$ [corresponding to $(v_{A\phi}/r\Omega)_c = 0.0175$] [left column; with $\omega = (0.9312 + i0.0018)\Omega_{\text{in}}$] or $b_\phi = 0.015$ [corresponding to $(v_{A\phi}/r\Omega)_c = 0.026$] [right column; with $\omega = (0.93 + i0.00065)\Omega_{\text{in}}$]. The solid and dotted curves show the total angular momentum flux and the flux carried by the fluid motion only (the Reynolds stress), respectively. The bottom panels are the blow-up of panel (b) near the magnetic resonances whose locations are indicated by the two vertical lines.

$$\Delta F = F(r_{\text{IMR}-}) - F(r_{\text{OMR}+}) = \Delta F_{\text{IMR}} + \Delta F_{\text{OMR}}. \quad (75)$$

Note that although both $|\Delta F_{\text{IMR}}|$ and $|\Delta F_{\text{OMR}}|$ are much larger (by orders of magnitude) than ΔF in the $B = 0$ case, the net jump ΔF is smaller for discs with finite B_ϕ . As B_ϕ increases, $|\Delta F_{\text{IMR}}|$ and $|\Delta F_{\text{OMR}}|$ both decrease, and ΔF becomes smaller and may even change sign (See Fig. 9). This decrease of wave absorption at the MRs due to finite magnetic fields results in a reduced or even diminished super-reflection (see Sec. 4), leading to a reduction of the growth rate and even stabilization of disc p-modes.

Figure 9 shows the p-mode growth rate as a function of b_ϕ and the corresponding net angular momentum jump across the CR/MRs region. Obviously, the decrease of ΔF with increasing b_ϕ directly correlates with the decrease of the mode growth rate. Note that when ΔF is zero or slightly negative, the p-mode still has a finite growth rate. This is because wave transmission across the corotation barrier always tends to increase the reflectivity [see Eq. (58)], thereby promoting the mode growth. With a further increase of b_ϕ , the mode growth becomes completely suppressed. For example, for discs with $c_s = 0.1r\Omega$, the angular momentum absorption at the CR/MRs change sign at $b_\phi = 0.0132$, while the mode growth rate becomes zero at $b_\phi \simeq 0.017$, or $(v_{A\phi}/c_s)_{\text{in}} \simeq 0.17$ [corresponding to $(v_{A\phi}/c_s)_c = 0.3$]. For discs with $c_s = 0.05r\Omega$, the mode growth rate vanishes at $b_\phi \simeq 0.01$, or $(v_{A\phi}/c_s)_{\text{in}} \simeq 0.2$ [corresponding to $(v_{A\phi}/c_s)_c = 0.34$].

Figure 10 shows the real and imaginary parts of the $m = 2$ mode frequency as a function of the dimensionless field strength $v_{A\phi}/(r\Omega)$ (evaluated at r_c) for different disc sound speeds and different values of q (measuring the slope of B_ϕ). Clearly, for such a small field strength, the real mode frequency is approximately independent of B_ϕ and q , since the propagation zone of the wave mode is hardly modified by the magnetic field. The mode growth rate, however, is significantly affected because of the modification to the CR. Not surprisingly, $\text{Im}(\omega)$ depends on B_ϕ mainly through the ratio $(v_{A\phi}/r\Omega)_c$.

5.2 Results for discs with mixed magnetic fields

The effects of vertical magnetic fields and mixed fields on the disc p-mode growth rate are illustrated in Fig. 11 and Fig. 12. We see that the real mode frequency depends very weakly on the field strength unless v_A becomes comparable to or larger than c_s . The solid line in Fig. 11b shows that for the pure vertical field case, the p-mode growth rate decreases with increasing B_z . This is consistent with our finding in Sec. 4.2 that a finite B_z tends to reduce the reflectivity (see Fig. 6). When the toroidal field is also included, we see the similar trend (see the dotted and dashed lines). Thus both vertical and toroidal magnetic fields tend to suppress the corotational instability. The effect of the toroidal magnetic field is somewhat larger than the vertical field, given that the required toroidal field strength B_ϕ to completely suppress the mode growth is smaller than

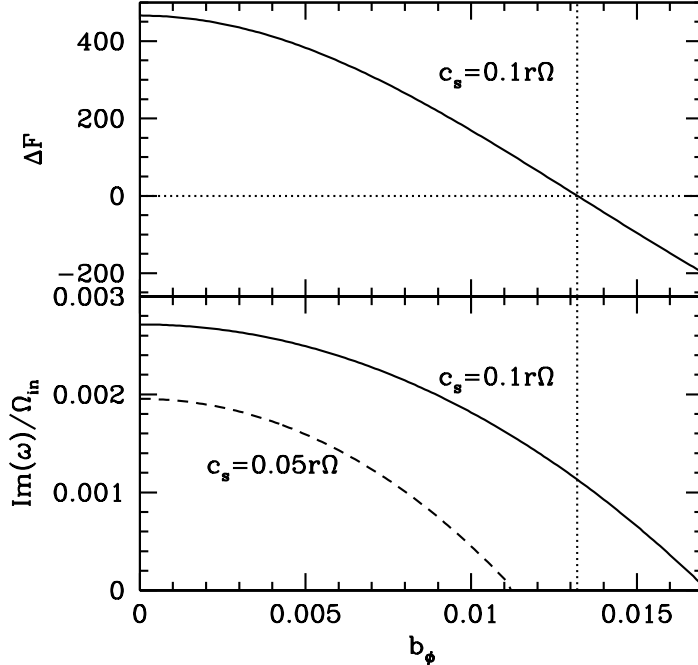


Figure 9. The net angular momentum flux jump across the two magnetic resonances (upper panel) and the mode growth rate (lower panel) as a function of the dimensionless toroidal magnetic field strength $b_\phi = (v_{A\phi}/r\Omega)_{\text{in}}$. The solid lines are for disc sound speed $c_s = 0.1r\Omega$, and the dashed line in the lower panel is for $c_s = 0.05r\Omega$. The other parameters are the same as in Figs. 5.1 and 8: $m = 2$, $\sigma = 1$, $q = 0$.

the required B_z . This is understandable since the p-modes have no vertical structure (with $k_z = 0$), and fluid motion in the disc does not directly bend the vertical field lines.

In Fig. 12, we compare the angular momentum flux profiles for the pure toroidal field case and the mixed field case. From the upper panel of this figure we see that for the mixed field case, the net flux jump across the resonance zone is smaller than the pure toroidal field case. This explains the somewhat smaller mode growth rate ($\omega_i/\Omega_{\text{in}} = 0.0017$) for the mixed field case as compared to the pure toroidal field case ($\omega_i/\Omega_{\text{in}} = 0.0018$). Note that the real part of the eigenfrequency is also modified slightly by the vertical field. This gives rise to the shift of “plateau” in the bottom panel of Fig. 12.

6 CONCLUSION

In this paper we have investigated the effects of magnetic fields on the corotational instability of the p-modes (also called inertial-acoustic modes for the $B = 0$ case) in BH accretion discs. These modes have no vertical structure, are trapped between the inner disc edge and the inner Lindblad resonance, and have the character of inertial-fast magnetosonic waves in their propagation zone. Previous works have shown that in a hydrodynamic disc (with $B = 0$) these modes can be overstable due to wave absorption at the corotation resonance (CR) when the vortensity (or its generalization for non-barotropic flows) of the disc has a positive gradient (TL08, LT09, Tsang & Lai 2009b). In this paper we found that the inclusion of a finite toroidal field B_ϕ splits the CR into two magnetic (slow) resonances (MRs), where the wave frequency in the rotating frame of the fluid, $\omega - m\Omega$, matches the slow magnetosonic wave frequency. At the inner and outer MRs, the angular momentum flux carried by the wave undergoes significant change, indicating angular momentum (and energy) absorption at both MRs. One of the resonances absorbs positive angular momentum while the other emits positive angular momentum. Independent of the background flow vortensity gradient, the net angular momentum absorption across the resonance region is always reduced or becomes more negative in discs with $B_\phi \neq 0$ compared to the $B = 0$ case. This leads to a reduced growth rate of the p-modes. Our calculations showed that the hydrodynamically overstable inertial-acoustic modes can be completely stabilized by the toroidal field at relatively small field strengths (see Fig. 10) For example, for discs with sound speed $c_s = 0.1r\Omega$, the $m = 2$ p-mode growth rate vanishes at $v_{A\phi}/(r\Omega) \sim 0.03$ (evaluated at the corotation radius r_c ; where $v_{A\phi} = B_\phi/\sqrt{4\pi\rho}$ is

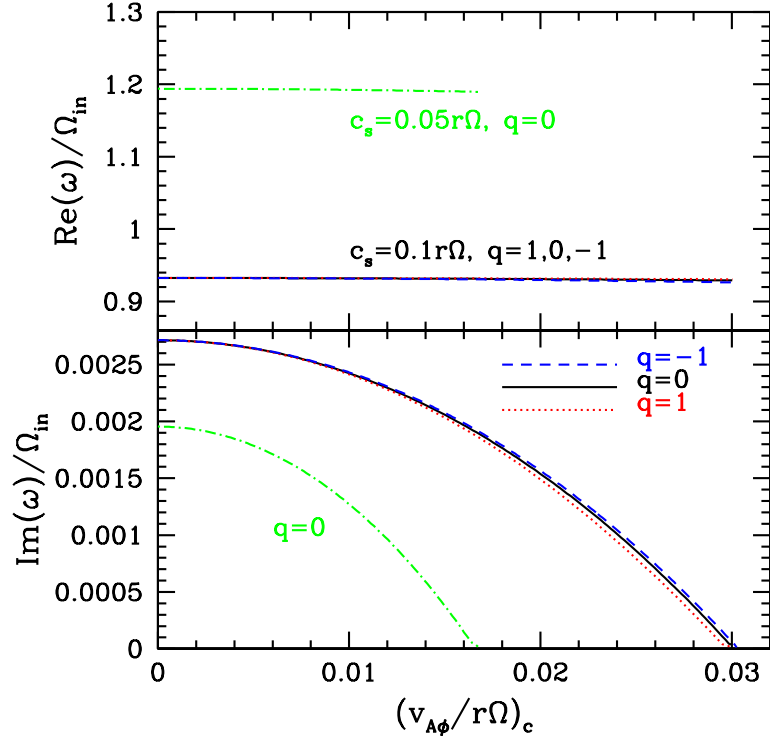


Figure 10. Frequencies of the $m = 2$ p-modes as a function of the dimensionless toroidal magnetic field strength, $(v_{A\phi}/r\Omega)_c$, with the upper and lower panels showing the real and imaginary parts, respectively. Different curves correspond to different values of $q = d \ln B_\phi / d \ln r$ (i.e., the slope of B_ϕ profile) and sound speed c_s . The disc density profile is $\rho \propto r^{-1}$, i.e. $\sigma = 1$.

the Alfvén speed associated with B_ϕ), corresponding to $(v_{A\phi}/c_s)_c \sim 0.3$. We also carried out numerical calculations of the reflectivity of a wave approaching the corotation from small radii. We showed that the reflectivity is reduced by the toroidal magnetic field, in agreement with our global mode calculation results.

For discs with a pure vertical field, the corotation resonance persists for the p-modes, with no additional magnetic resonances. This is understandable since p-modes have no vertical structure ($k_z = 0$). With no bending of the field lines, the vertical field simply modifies the background pressure, or equivalently, changes the effective background sound speed. However, when $B_z \neq 0$, the effective potential for wave propagation contains a second-order singularity term, in addition to the first-order singularity already present in a $B_z = 0$ disc.

For discs containing mixed (toroidal and vertical) magnetic fields, the corotation resonance is split into four resonances: in addition to the inner/outer MRs (already present in discs with pure toroidal fields), two Alfvén resonances appear, where $\omega - m\Omega$ matches the local Alfvén wave frequency. We showed that the effect of these additional resonances is to further reduce the super-reflection and the growth rate of the disc p-modes (see Fig. 11). Overall, the toroidal field has a larger effect on the corotational wave absorption and the mode growth rate than the vertical field.

The main finding of our paper is that overstable non-axisymmetric p-modes tend to be stabilized by disc magnetic fields. This implies that, in order for p-modes to explain HFQPOs observed in black-hole X-ray binaries, the disc magnetic field must be sufficiently weak (with the magnetic pressure appreciably less than the thermal pressure) so that the corotational instability is not completely suppressed. Alternatively, some other mode excitation mechanisms are needed. One possibility could be mode excitations by turbulent viscosity (see Kato 2001 for a general discussion of viscous driving of disc oscillation modes) or by vorticity perturbations associated with the turbulence (see Heinemann & Papaloizou 2009). Another possibility could be the accretion-ejection instability studied by Tagger et al. (see Tagger & Pellat 1999; Varniere & Tagger 2002; Tagger & Varniere 2006), which involves large-scale equipartition vertical magnetic fields threading a thin disc embedded in a vacuum or a tenuous corona. Whether these other possible excitation mechanisms can compete with the stabilizing effects of the internal disc magnetic fields remains to be studied. Nevertheless, our finding is limited by the fact that the disc model we considered is essentially an infinite cylinder without vertical structure, whereas in reality disc background (density, magnetic field, etc.) varies in vertical direction. More realistic disc models certainly need to be investigated in future studies.

Finally, we note that although in this paper we have studied the role of magnetic fields in the context of black-hole

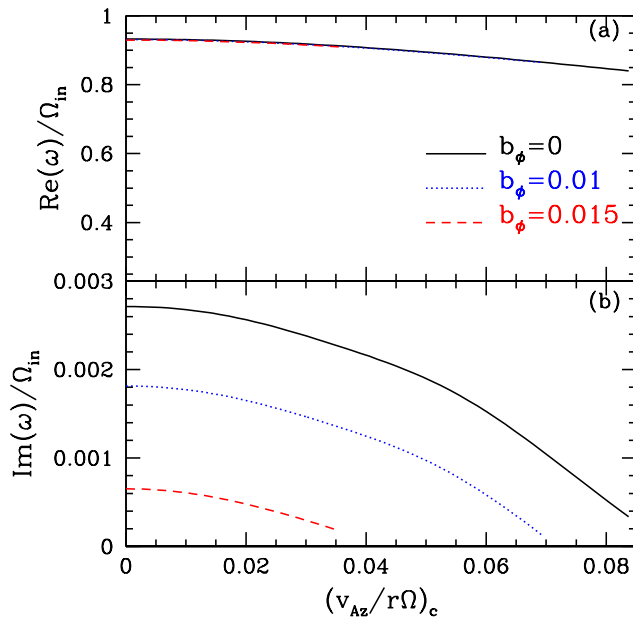


Figure 11. Frequencies of the $m = 2$ p-modes as a function of the dimensionless vertical magnetic field strength, $(v_{Az}/r\Omega)_c$, with the upper and lower panels showing the real and imaginary parts, respectively. Different curves correspond to different values of the disc toroidal fields. Note that the real mode frequency depends weakly on the magnetic field (for the range of field strength considered), thus $b_\phi = 0.01$ corresponds to $(v_{A\phi}/r\Omega)_c \simeq 0.0175$ and $b_\phi = 0.015$ corresponds to $(v_{A\phi}/r\Omega)_c \simeq 0.026$. The other disc parameters are: $\sigma = 1$, $q = 0$ and $c_s = 0.1r\Omega$.

diskoseismic oscillations and QPOs, the dynamical effects of magnetic fields on the corotation resonance examined here are quite general. Our finding in this paper suggests that dynamical instabilities in other rotating astrophysical flows where the corotation resonance plays an important role may be significantly affected by magnetic fields. Examples include the Papaloizou-Pringle instability in accretion tori and the global rotational instability in differentially rotating stars. We will study some of these issues in separate papers (Fu & Lai 2010).

ACKNOWLEDGMENTS

We thank Thierry Foglizzo, Michel Tagger and especially David Tsang for useful discussion during the course of this study. We are grateful to an anonymous referee whose comments helped improve this manuscript. This work has been supported in part by NASA Grant NNX07AG81G and NSF grants AST 0707628. DL also acknowledges the hospitality (Jan – Jun, 2010) of the Kavli Institute for Theoretical Physics at UCSB, funded by the NSF through grant PHY05-51164.

REFERENCES

- Arras, P., Blaes, O. & Turner, N. J., 2006, *ApJ*, 645, L65
- Balbus, S. A. & Hawley, J. F., 1998, *Rev. Modern Phys.*, 70, 1
- Baruteau, C. & Masset, F., 2008, *ApJ*, 672, 1054
- Blokland, J. W. S., van der Swaluw, E., Keppens, R. & Goedbloed, J. P., 2005, *A&A*, 444, 337
- Bondeson, A., Iacono, R. & Bhattacharjee, A., 1987, *Phys. Fluids*, 30, 2167
- Brandenburg, A., Nordlund, A., Stein, R. F. & Torkelsson, U., 1995, *ApJ*, 446, 741
- Davis, S. W., Stone, J. M. & Pessah, M. E., 2010, *ApJ*, 713, 52
- Done, C., Gierlinski, M. & Kubota, A., 2007, *A&AR*, 15, 1
- Feng, H., Rao, F. & Kaaret, P., 2010, *ApJ*, 710, L137
- Ferreira, B. T. & Ogilvie, G. I., 2008, *MNRAS*, 386, 2297
- Frieman, E. & Rotenberg, M., 1960, *Rev. Modern Phys.*, 32, 898
- Fromang, S., 2010, *A&A*, 514, L5
- Fromang, S., Terquem, C. & Nelson, R. P., 2005, *MNRAS*, 363, 943

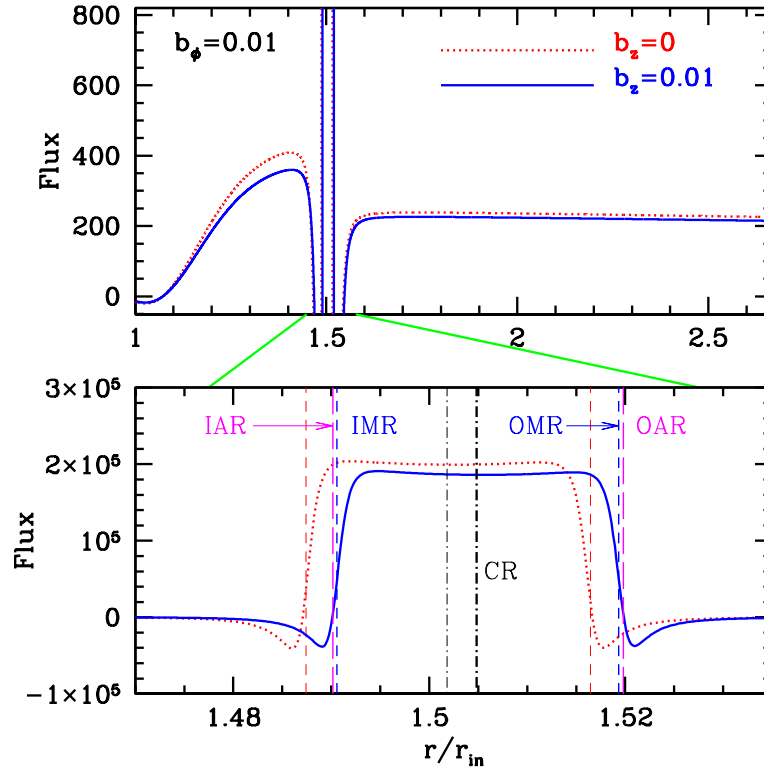


Figure 12. The angular momentum flux carried by wave modes as a function of radius in a BH accretion disc with mixed magnetic fields. The bottom panel is the zoom-in of the upper panel near the resonances. The dotted curves are for a disc with a pure toroidal field, while the solid curves are for a disc with both toroidal and vertical fields. The short-dashed vertical lines indicate the inner and outer magnetic slow resonances (IMR and OMR). The dot-dashed vertical lines represent the corotation resonance (CR). The long-dashed vertical lines (very close to the short-dash lines) indicate the inner/outer Alfvén resonances (IAR and OAR) which only exist in the mixed field case. Note that the mode frequency in the $b_z = 0$ case is different from the $b_z = 0.01$ case, thus there is a slight shift in location of the MRs and CR between the two cases. Note that $b_\phi = 0.01$ and $b_z = 0.01$ correspond to $(v_{A\phi}/r\Omega)_c = (v_{Az}/r\Omega)_c = 0.0176$. The other disc parameters are: $\sigma = 1$, $q = 0$ and $c_s = 0.1r\Omega$.

- Fu, W. & Lai, D., 2009, *ApJ*, 690, 1386
 Fu, W. & Lai, D., 2010, *MNRAS*, accepted
 Gierlinski, M., Middleton, M., Ward, M. & Done, C., 2008, *Nature*, 455, 369
 Guan, X., Gammie, C. F., Simon, J. B. & Johnson, B. M., 2009, *ApJ*, 694, 1010
 Goldreich, P. & Tremaine, S., 1979, *ApJ*, 233, 857
 Goossens, M., Hollweg, J. V. & Sakurai, T., 1992, *Solar Physics*, 138, 233
 Hameiri, E., 1981, *J. Math. Phys.*, 22, 2080
 Hawley, J. F., Gammie, C. F., & Balbus, S. A., 1995, *ApJ*, 440, 742
 Heinemann, T. & Papaloizou, J. C. B., 2009, *MNRAS*, 397, 52
 Hirose, S., Blaes, O. & Krolik, J. H., 2009, *ApJ*, 704, 781
 Kato, S., 2001, *PASJ*, 53, 1
 Kato, S., 2003a, *PASJ*, 55, 257
 Kato, S., 2003b, *PASJ*, 55, 801
 Kato, S., 2008, *PASJ*, 60, 1387
 Keppens, R., Casse, F. & Goedbloed, J. P., 2002, *ApJ*, 569, L121
 Lai, D. & Tsang, D., 2009, *MNRAS*, 393, 979
 Latter, H. N. & Balbus, S. A., 2009, *MNRAS*, 399, 1058
 Li, L., Goodman, J. & Narayan, R., 2003, *ApJ*, 593, 980
 Longaretti, P. -Y., & Lesur, G., 2010, *A&A*, 561, A51
 Lovelace, R. V. E., Li, H., Colgate, S. A. & Nelson, A. F., 1999, *ApJ*, 513, 805
 Lovelace, R. V. E., Rothstein, D. M. & Bisnovatyi-Kogan, G. S., 2009, *ApJ*, 701, 885
 Middleton, M. & Done, C., 2010, *MNRAS*, 403, 9

- Middleton, M., Done, C., Ward, M., Gierlinski, M. & Schurch, N., 2009, MNRAS, 394, 250
- Mikhailovskii, A. B., Fridman, A. M., Churikov, A. P., Pustovitov, V. D. & Smolyakov, A. I., 2009, Plasma Phys. Controlled Fusion 51, 045003
- Miller, K. A. & Stone, J. M., 2000, ApJ, 534, 398
- Muto, T., Machida, M. N. & Inutsuka, Shu-ichiro, 2008, ApJ, 679, 813
- Narayan, R., Goldreich, P. & Goodman, J., 1987, MNRAS, 228, 1
- Nowak, M. A. & Wagoner, R. V., 1991, ApJ, 378, 656
- Okazaki, A. T., Kato, S. & Fukue, J., 1987, PASJ, 39, 457
- O'Neill, S. M., Reynolds, C. S. & Miller, M. C., 2009, ApJ, 693, 1100
- Paczynski, B. & Wiita, P. J., 1980, A&A, 88, 23
- Pessah, M. E., Chan, C. & Psaltis, D., 2006, MNRAS, 372, 183
- Pessah, M. E. & Goodman, J., 2009, ApJ, 608, L72
- Press, W. H., Teukolsky, S. A., Vetterling, W. T. & Flannery, B. P., 1992, Numerical Recipes, Cambridge University Press
- Remillard, R. A. & McClintock, J. E., 2006, ARAA, 44, 49
- Reynolds, C. S. & Miller, M. C., 2009, ApJ, 692, 869
- Sakurai, T., Goossens, M. & Hollweg, J. V., 1991, Solar Physics, 133, 227
- Silbergleit, A. S. & Wagoner, R. V., 2008, ApJ, 680, 1319
- Simon, J. B., Hawley, J. F. & Beckwith, K., 2009, ApJ, 690, 974
- Sorathia, K. A., Reynolds, C. S. & Armitage, P. J., 2010, ApJ, 712, 1241
- Stone, J. M., Hawley, J. F., Gammie, C. F. & Balbus, S. A., 1996, ApJ, 463, 656
- Strohmayer, T. E. & Mushotzky, R. F., 2009, ApJ, 703, 1386
- Swank, J., 1999, Nucl. Phys. B, Proc. Suppl., 69, 12
- Tagger, M. & Pellat, R., 1999, A&A, 349, 1003
- Tagger, M. & Varniere, P., 2006, ApJ, 652, 1457
- Tassev, S. V. & Bertschinger, E., 2007, ApJ, 686, 423
- Terquem, C. E. J. M. L. J., 2003, MNRAS, 341, 1157
- Tsang, D. & Lai, D., 2008, MNRAS, 387, 446
- Tsang, D. & Lai, D., 2009a, MNRAS, 393, 992
- Tsang, D. & Lai, D., 2009b, MNRAS, 400, 470
- Varniere, P. & Tagger, M., 2002, A&A, 394, 329
- Wagoner, R. V., 1999, Phys. Rep., 311, 259
- Yu, C. & Li, H., 2009, ApJ, 702, 75
- Zhang, H. & Lai, D., 2006, MNRAS, 368, 917